J. Space Weather Space Clim. 2025, **15**, 12

https://doi.org/10.1051/swsc/2025005

JSWSC

Available online at:
www.swsc-journal.org

TECHNICAL ARTICLE OPEN ACCESS

# High precision, high time-cadence measurements of the Mg II index of solar activity by the GOES-R Extreme Ultraviolet Irradiance Sensor 1: EUVS-C design and preflight calibration

William E. McClintock, Martin Snow[1,2,3], David Crotser[1], and Francis G. Eparvier[1]

[1] Laboratory for Atmospheric and Space Physics (LASP), University of Colorado, Boulder, CO 80309, USA
[2] South African National Space Agency (SANSA), Hospital Street, 7200 Hermanus, South Africa
[3] Department of Physics and Astronomy, University of the Western Cape, Robert Sobukwe Road, 7535 Bellville, South Africa

Received 25 September 2024 / Accepted 24 February 2025

**Abstract** – EUVS-C is one component of the Extreme Ultraviolet Irradiance Sensor (EUVS) instrument. EUVS, together with the X-Ray Sensor (XRS), comprise the Extreme Ultraviolet and X-ray Irradiances Sensors (EXIS) investigation aboard the GOES-R satellite series, which includes GOES-16, -17, -18, and -19. From their vantage points in geostationary orbit, the EUVS-C instruments make high-precision (better than 1 part in $10^4$), high-time-cadence (3 s) measurements of the solar Mg II Index with moderate (0.1 nm) spectral resolution. The index, also referred to as the Mg II core-to-wing ratio, is a proxy for chromosphere activity that correlates with solar extreme ultraviolet (EUV) irradiance. Mg II produces two bright chromosphere emission lines in the sun's spectrum at 279.55 nm and 280.71 nm (Mg II *k* and *h*) that appear in the cores of their respective photospheric absorption lines. Measuring the ratio of emission from the core (chromospheric) to that from the wings (photospheric) provides an index that is relatively insensitive to changes in radiometric performance that often occur when scientific instruments observe the sun. EUVS-C design specifications were informed by earlier research reporting index variability of approximately 0.2% on time scales of 6–10 min, increasing to approximately 0.3% and approximately 0.55% for 30 and 80 min, respectively. This paper describes the EUVS-C instrument design and implementation, its ground calibration and characterization, and its anticipated measurement performance. A companion paper describes the initial EUVS-C flight measurement performance.

**Keywords:** MgII Index / Solar activity

## 1 Introduction and science motivation

The Extreme Ultraviolet Irradiance Sensor Channel C (EUVS-C, Snow et al., 2009), which provides real-time, high-cadence (3 s), high-precision (1 part in $10^4$) operational measurements of the Mg II core-to-wing ratio (Heath & Schlesinger (1986)), is one component of the Extreme Ultraviolet Irradiance Sensor (EUVS) instrument (Eparvier et al., 2009). EUVS, together with the X-Ray Sensor (XRS), comprise the Extreme Ultraviolet and X-ray Irradiances Sensors (EXIS) investigation (Machol et al., 2020) aboard the GOES-R satellite series, which includes GOES-16, -17, -18, and -19. Two GOES satellites are operational at any one time, and from their vantage points in geostationary orbit at 75.2° west longitude (GOES-16 or GOES-19) and 137.2° west longitude (GOES-17 or GOES-18), the EXIS instruments measure solar radiation and its variability at X-ray, extreme ultraviolet (EUV), far ultraviolet (FUV) and middle ultraviolet (MUV) wavelengths. This article describes the design and pre-launch calibrations of EUVS-C. Woods et al. (2024) discuss the EXIS XRS instrument.

EUVS-C observes a narrow range of MUV wavelengths (~275–284 nm), which is centered around the Mg II *k* and *h* lines at 279.64 nm and 280.35 nm (vacuum values), respectively. Emissions from the centers (cores) of the *k* and *h* lines originate in the chromosphere and exhibit significant short-term (27-day solar rotation time scales) and long-term (11-year solar cycle time scales) variability. Heath & Schlesinger (1986) pointed out that emission at wavelengths a few nm distant from the line centers originates in the sun's photosphere, and is, therefore, much less variable than that from the chromosphere. This idea is illustrated in Figure 1. The left panel compares portions of two 0.1 nm resolution spectra containing the

*Corresponding author: william.mcclintock@colorado.edu

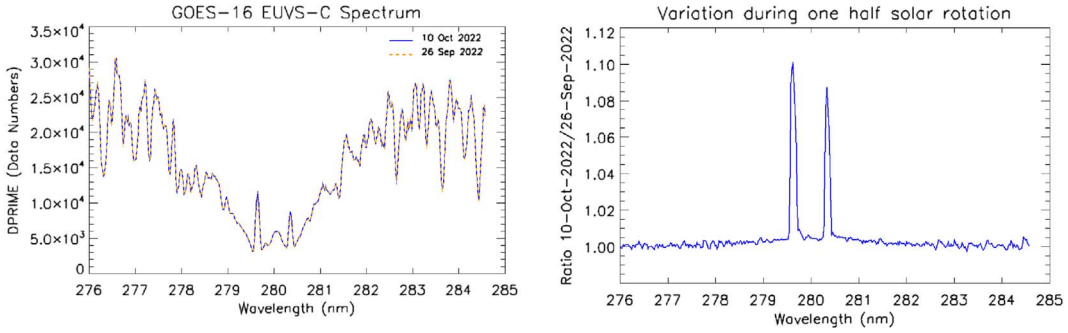


**Figure 1.** Example EUVS-C Observations. Left: spectra with 0.1 nm resolution plotted in corrected data numbers collected during a 3-second integration (DPRIME, see Sect. 5.2) for two dates 14 days apart (half a solar rotation). These dates were chosen because there was a single large active region on the solar disk that rotated into view on October 10, 2022. Right: ratio of the spectra shown on the left panel. Strong variability is evident in the *h* and *k* emission lines relative to adjacent wavelengths.

Mg II *k* and *h* lines recorded by EUVS-C aboard the GOES-16 spacecraft. One is from September 20, 2022 (orange dashed), and the other is from a day with high solar activity [(October 10, 2022 (blue)] that is separated in time from the first by half a solar rotation. The right panel shows the ratio of those two observations. Strong variability is evident in the *h* and *k* emission lines relative to adjacent wavelengths.

The left panel of Figure 2 shows the time series of the composite MgII index from the University of Bremen group (https://www.iup.uni-bremen.de/UVSAT/data/). Colors in the plot correspond to the different instruments used to create the index. Each instrument in the composite is scaled to match the previous instruments. The data in Figure 2 has been scaled to match the published NOAA standard (Viereck et al., 2004). These plots show clear evidence of index variability on both solar cycle and solar rotation time scales.

Using 1.1 nm spectral resolution data from the Solar Backscattered Ultraviolet (SBUV) experiment on Nimbus 7, Heath & Schlesinger defined a "Mg II Index" as the ratio of emission in the cores of the lines to that of two wavelengths on either side of the line center

$$\mathrm{MgII}_{\mathrm{SBUV}} = \frac{4 \cdot [I_{279.8} + I_{280.0} + I_{280.2}]}{3 \cdot [I_{276.6} + I_{276.8} + I_{283.2} + I_{283.4}]}. \quad (1)$$

This index, after appropriate scaling, successfully represented both the short-term and long-term variability for far ultraviolet (<204 nm) solar spectral irradiance. Subsequently, Mg II index variation has been shown to be an excellent proxy for variations in EUV radiation in the 25–35 nm wavelength range (Viereck et al., 2001) and generally as a predictor of solar spectral irradiance variability (Dudok de Wit et al., 2009; Wintoft, 2011; Yeo et al., 2017; Coddington et al., 2019; Chamberlin et al., 2020; Lean et al., 2020). Figure 3 shows the correlation between a single ultraviolet wavelength (upper left) and the correlation coefficient for all MUV wavelengths (upper right) observed by the Spectral Irradiance Monitor (SIM) on the Total and Spectral Irradiance Sensor-1 (TSIS-1, Richard et al., 2024). The decrease in correlation from 97% to 87% for wavelengths longer than 280 nm due to radiative transfer effects in the solar atmosphere. The formation height of the longer wavelengths is below the chromosphere, and the variation in those wavelengths shows an increasing contribution from photospheric sources, i.e., the sunspot blocking factor in empirical models such as Coddington et al. (2016). Figure 11 from Lean et al. (1997) shows a similar change in correlation using UARS/SOLSTICE measurements. The variability of the MgII index is highly correlated with EUV irradiances as well (Viereck et al., 2001), as shown in the two lower panels of Figure 3, and produces a more accurate model of thermospheric density (Thuillier & Bruinsma, 2001).

The 1.1 nm spectral resolution available in the SBUV instruments was not sufficient to resolve the individual *k* and *h* emission cores, which require $\Delta\lambda \sim 0.2$ nm. Today, there are several satellite instruments with that capability, including the Global Ozone Monitoring Experiment (GOME-2B and GOME-2C; Burrows et al., 1999; Otter et al., 2017) with $\Delta\lambda = 0.17$ nm. The SOLar-STtellar Irradiance Comparison Experiment (SOLSTICE, McClintock et al., 2005) onboard the Solar Radiation and Climate Experiment (SORCE, Rottman, 2005) and the EUVS-C have a resolution of $\Delta\lambda = 0.1$ nm. SOLSTICE observed from 2003 to 2020. Additionally, the Interface Region Imaging Spectrograph (IRIS, De Pontieu et al. 2014) provides observations of selected regions of the solar disk with $\Delta\lambda = 0.0025$ nm per pixel. Although it is not a spectrograph, the Solar Ultraviolet Imaging Spectrograph (SUIT) onboard the Aditya-L1 spacecraft provides spatially resolved indices using filters that spectrally isolate the Mg II wings and emission cores (Ghosh et al., 2016). Work to intercompare the spectroscopic result from the various instruments is ongoing (e.g., Snow et al., 2014, 2018).

Because the Mg II index is a ratio measurement, it is largely, but not completely, insensitive to long-term changes in instrument sensitivity (Snow et al., 2019). Even wavelength-dependent changes in sensitivity can be tolerated as long as they can be approximated as linear across the ~7 nm wavelength range used to calculate the index. This is an important advantage over the measurement of absolute solar spectral irradiance variability, particularly at ultraviolet wavelengths (Heath & Schlesinger, 1986). Maintaining long-term knowledge of the radiometric accuracy of an instrument in space is challenging because exposure of optics and detectors to the sun leads to degradation in responsivity that is very difficult to predict or accurately measure. Researchers have adopted various approaches for mitigating this issue, including using in-flight calibration lamps (Brueckner et al., 1993), duty-cycling identical

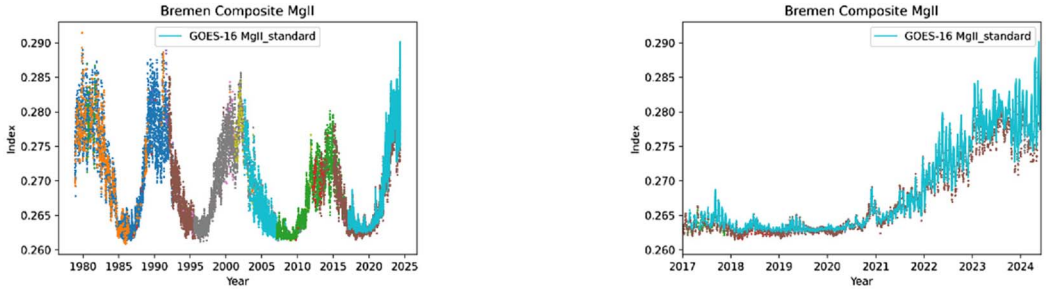


**Figure 2.** EUVS-C observations as part of the long-term composite record. The full-time series is shown on the right panel, while the left panel shows only the time period beginning with GOES-16.

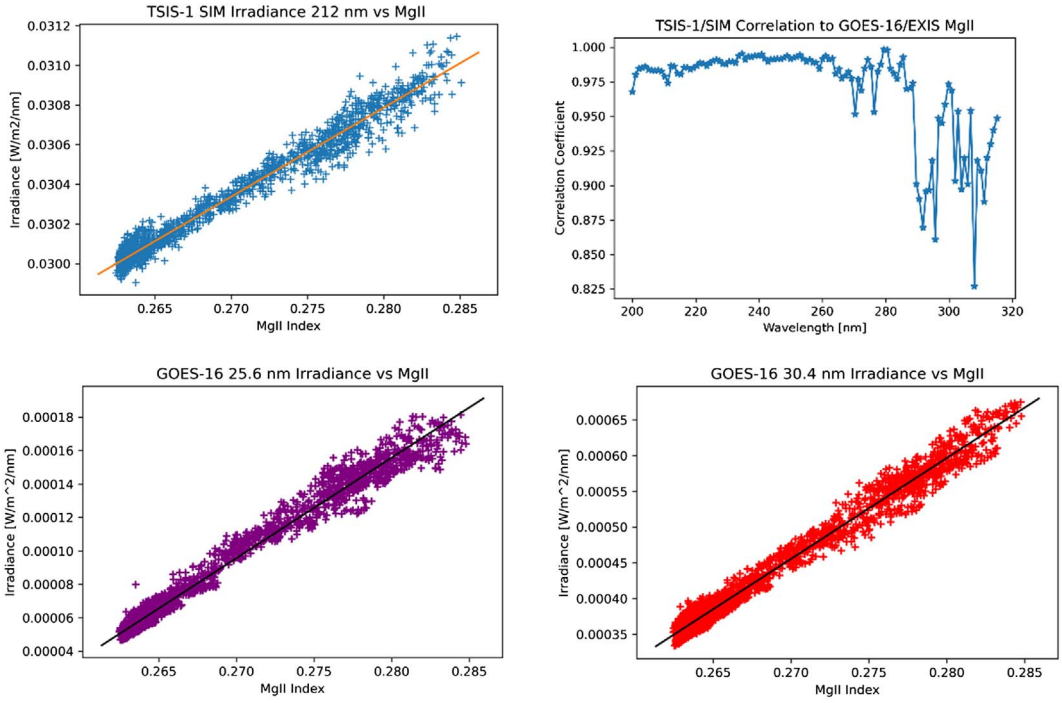


**Figure 3.** (upper left) Correlation between one MUV wavelength observed by TSIS-1/SIM and the EUVS-C Mg II index. The irradiance is highly linearly correlated to the index. (upper right) The Pearson correlation coefficient for all MUV wavelengths observed by TSIS-1/SIM. Lower panels show the Index correlation with EUV irradiances 25.6 nm (lower left) and 30.4 nm (lower right). Their Pearson correlation coefficients are 0.9901 and 0.9897, respectively,

instruments to manage relative exposure (Richard et al., 2012), and comparing observations by identical instruments made from sounding rockets (Woods et al., 2012). EUVS-C employs periodic off-pointing (four times a year) that places the solar image on a normally unused region of the optical system to track radiometric performance (McClintock et al., 2025).

### 1.1 Summary of the Mg II Index characteristics

The general spectral shape of the solar spectrum in the wavelength range shown in Figure 1 is determined by the two overlapping Mg II absorption lines (air wavelengths 279.64 nm and 280.35 nm) that originate in the photosphere. Numerous weaker photospheric Fraunhofer features also appear. The two peaks near the absorption line centers are the chromospheric emission components. They are strongly variable on both 27-day solar rotation time scales during solar maximum and on 11-year solar cycle time scales. Figure 4 compares a full disk high-resolution ($\Delta\lambda \sim 0.0025$ nm) spectrum surrounding the *k* and *h* lines measured by IRIS (Kayshap et al., 2018) with a 0.01 nm – resolution spectrum obtained with a balloon-borne spectrograph (Hall & Anderson, 1988, 1991). The IRIS spectrum reveals self-reversed profiles with an approximate 0.11 nm full-width-at-the-base that are superimposed on their photospheric lines, which appear to have non-zero residual emission at the line center. Although similarity in line shapes between IRIS and the balloon suggests that 0.01 nm is adequate to separate the *k* and *h* emission cores from their surrounding continua, IRIS more completely resolves their central reversals. Also included in Figure 4 are the results of

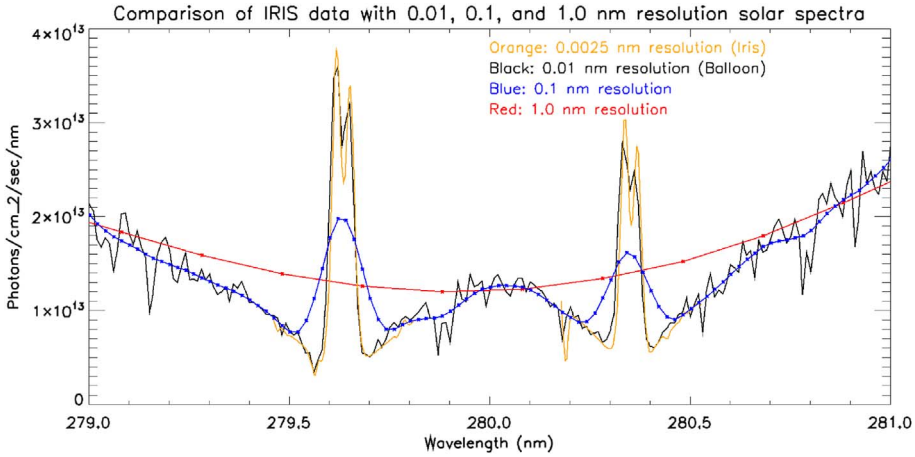


**Figure 4.** Representative spectra from a balloon-borne spectrograph (black) and IRIS (orange). Whereas the strengths of the *k* and *h* emission lines vary for these spectra because they were acquired at different epochs, the continua are similar because they arise from the relatively constant photosphere. The smooth blue and red curves are convolutions of the balloon spectrum with 0.1 nm and 1.0 nm FWHM triangular response functions, respectively.

convolving the balloon spectrum with a 0.1 nm full width at half maximum (FWHM) triangular response function sampled at 0.02 nm wavelength spacing and a 1.0 nm FWHM spectrum sampled at 0.2 nm spacing. Photosphere and chromosphere components are partially and strongly mixed in spectra with ~ 0.1 nm and ~1 nm resolution, respectively.

The ratio of spectra shown in the right panel of Figure 1 indicates that chromospheric emission drives variability within ±0.05 nm of the line center. There is also measurable (approximately 0.5%) variability near the line center in the photospheric lines. This increases to approximately 2% on solar cycle time (Snow et al., 2022). Inspection of time series of daily irradiance measurements at 276.5 ± 0.5 nm and 283.5 ± 0.5 nm using Ozone Monitoring Instrument (OMI; Marchenko et al., 2019) data and SOLSTICE data corrected using the Multi Same-Irradiance-Level analysis technique (Woods et al., 2018) indicate that solar cycle variations in these 1-nm bins is less than 1%, consistent with results discussed by Coddington et al. (2019).

Using moderate-cadence observations from SORCE/SOLSTICE (Snow et al., 2005), estimated that the uncertainty in the SOLSTICE Mg II index was 0.65%, and the daily distribution of measurements relative to the mean could be fit with a normal distribution with a FWHM of 1.2%. Those results were for observations during the declining phase of solar cycle 23, i.e., moderate solar activity. During solar minimum, the variation over the day is on the order of 0.2%. This sets an upper limit to the required repeatability to measure intra-day variability at all solar activity levels.

### 1.2 Mg II Index precision

A limitation of the 1.1 nm resolution SBUV index is relatively low contrast $(I_{MAX}–I_{MIN})/I_{Mean}$ where $I_{MAX}$, $I_{MIN}$, and $I_{Mean}$ are maximum, minimum, and mean values, respectively, that arises because the numerator in equation (1) contains both the chromospheric core and a significant contribution from the wings of the photospheric line. Using 0.24 nm resolution data from the SOLSTICE investigation aboard the UARS satellite (Rottman et al., 1993), De Toma et al. (1997) and White et al. (1998) explored the effects of increased resolution on the properties of the Mg II index. They defined a new index where the numerator contained the total emission in two 0.36 nm-wide wavelength bands centered on *h* and *k* and the denominator was the average of the maxima of parabolic fits to four 0.5 nm wide bins in the wings centered on 276.1 nm, 276.6 nm, 283.2 nm, and 283.9 nm. This index, which contained smaller contributions from the photosphere, resulted in a factor of 2.2 increase in contrast and captured more solar activity during the 1996 solar minimum. White et al. (1998) concluded that both indices showed a reduction in rotational variability near solar minimum.

Snow et al. (2005) studied the impacts of spectral resolution and signal-to-noise ratio (SNR) on the index using 0.1 nm resolution data from SORCE SOLSTICE (McClintock et al., 2005). They replaced the UARS-SOLSTICE wing definition (De Toma et al., 1997) with the original SBUV 1.1 nm resolution definition:

$$\mathrm{Mg\,II}_{\mathrm{SORCE/SOLSTICE}} = \frac{2 \cdot [I_k + I_h]}{[I_{276.6} + I_{276.8} + I_{283.2} + I_{283.4}]}. \quad (2)$$

Wing irradiances were calculated by convolving the full-resolution spectrum with a triangular, 1.1 nm (FWHM) response function sampled at 0.2 nm. These were summed at the 4 SBUV wavelengths. Core radiances were computed by fitting Gaussian functions to *h* and *k*, respectively, and integrating them. The effective integration range was approximately ±0.08 nm about each line center and the result contained any residual emissions from the photosphere in those bands. This was compared to a low-resolution index calculated using the 1.1 nm smoothed data and the SBUV index defined by equation (1). The result of this new definition was a factor of 7 increase in contrast relative to the SBUV index. Additionally, Snow et al. showed that the relative uncertainty in the SORCE index for a single scan was ~0.6% compared to 1.23% for the UARS index. In addition to solar-cycle and rotational time scales, they investigated index fluctuations throughout a single day and showed that the SORCE index exhibited daily 1$\sigma$ fluctuations of ~1% about

the mean during January–February 2004. These were easily detected using the SORCE index but were masked by measurement noise using the low-resolution index.

Snow & McClintock (2005) used SORCE SOLSTICE data taken in standard mode (one solar spectrum covering 180–320 nm every 25 min with a sampling of 0.034 nm and an integration time of 0.5 s per wavelength bin, respectively), which had a relative index measurement error of 0.35%, to show that Mg II $_{\text{SORCE/SOLSTICE}}$ fluctuates ~1% 1-$\sigma$ in a typical 24-hour period. They also investigated index variability on time scales less than a day using special "rapid – scan" mode data, which covered just the cores of the emission lines in 45 s with a sampling of 0.011 nm that produced an index measurement error of 0.05%. The results revealed index variability of approximately 0.2% on time scales of 6–10 min, increasing to approximately 0.3% and approximately 0.55% for 30 and 80 min, respectively. Whereas daily variation might be attributed to active regions rotating in and out of view, those seen on shorter timescales likely represent true variability within the active regions and chromospheric network that give rise to the observed emission. These findings indicate that the ideal instrument for measuring the full intrinsic variability of Mg II chromospheric variability on timescales of tens of minutes and longer should be designed to achieve approximately 0.1% precision with a 1-minute cadence or better. These constraints set the primary measurement requirements for EUVS-C.

## 2 Measurement and implementation requirements

### 2.1 Measurement requirements

Snow & McClintock (2005) investigated the effects of spectral resolution and spectral sampling on the precision of the Mg II index with the goal of defining measurement parameters for the EUVS-C. They assumed an instrument with radiometric performance comparable to SORCE SOLSTICE (A single measurement of a 0.1 nm wide spectral bin at the wavelength of peak emission in each wing provides SNR of approximately 150) and used Monte Carlo simulations of SOLSTICE Mg II spectra to construct the curves of constant measurement precision illustrated in Figure 5. This analysis led to the final selection of 0.1 nm and 5 samples per resolution element for EXIS-C spectral resolution and sampling, respectively. Snow & McClintock (2005) also studied long-term trends in wing irradiances in two 1 nm bands located between 1 nm and 3 nm from Mg II line center. They concluded that the wavelength intervals selected for the original SBUV index exhibited less solar cycle variability than intervals closer to the chromosphere emission line centers. This result was previously demonstrated by Deland & Cebula (1994) using SBUV discrete mode measurements. Thus, EUVS-C was designed to cover the entire spectral range defined by the SBUV index. Table 1 captures the measurement performance requirements that drove the instrument design.

### 2.2 Implementation requirements

In addition to measurement requirements, the EUVS-C design was constrained by the following implementation requirements:

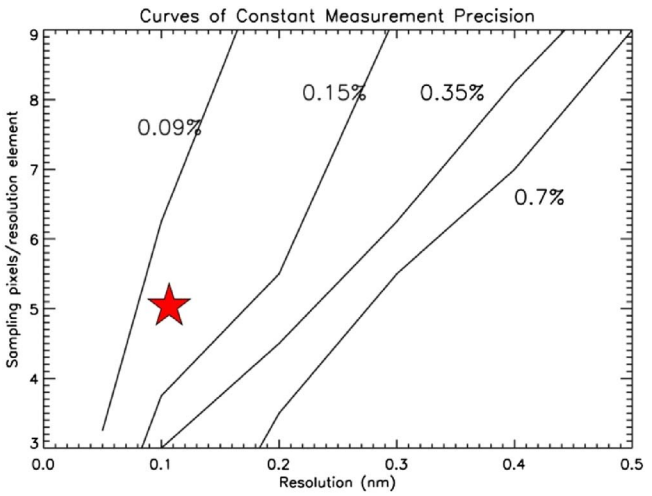


**Figure 5.** Curves of constant measurement precision as a function of spectral resolution and spectral sampling. A red star marks the values of these performance parameters selected for the EUVS-C.

- Radiation damage tolerance: EXIS operates in geostationary orbit and is built to tolerate a radiation environment with energetic trapped electrons and protons and solar protons with energies up to 10 MeV and 100 MeV, respectively. Radiation damage is controlled using a combination of aluminum and tungsten shielding for sensitive electronic and optical components and for detectors.
- Solid state CMOS array detector: The original SBUV and SOLSTICE instruments were scanning monochromators that employed photomultiplier tube detectors requiring high voltage. The use of silicon-based array detectors removes the requirement for a precision scanning mechanism, and the solid-state architecture eliminates the requirement for high voltage operation associated with a microchannel plate (MCP)-based architecture. Solid state detectors are inherently more radiometrically stable as well, but they are very sensitive to visible light and require substantially more optical shielding than MCPs, which can be fabricated with vanishingly small visible sensitivity. Snow & McClintock (2005) compared the performance of both CCD-based and CMOS-based detectors for use in a Mg II monitor similar to EUVS-C. They concluded that the CCD detector had significantly lower read noise. However, both detectors met the measurement requirements summarized in Table 1. Therefore, CMOS technology was selected for EUVS-C based on its higher tolerance to radiation-induced dark current and the ease of implementing readout electronics.
- Redundant design: The GOES lifetime requirement of up to 10 years of operation after potentially 10 years of storage was met by implementing an EUVS-C design that includes two fully redundant optical-detector channels referred to as C1 and C2. Based on pre-launch test results, one channel is chosen as operational in flight. The other is held in reserve. To date, none of the reserve channels have observed the Sun. The current state of their calibration is unknown.

**Table 1.** EUVS-C measurement requirements.

| Parameter | Value | Comments |
|---|---|---|
| Spectral resolution | 0.1 nm | Resolve emission cores |
| Spectral sampling | 0.02 nm | 5 samples per resolution element |
| Wavelength coverage | 275–284.5 nm | Capture full range of the SBUV index |
| Field of view | > 40 arc minutes circular | 2° × 2° Nominal design |
| Cadence | 1 minute or less | Capture Mg II index variability on 10-minute time scales |
| Radiometric precision | SNR > 150 average @ 277 nm | Measure index with 0.1% precision |
| Detector radiation exposure | < 15 krad over mission lifetime | Tungsten and aluminum shielding |

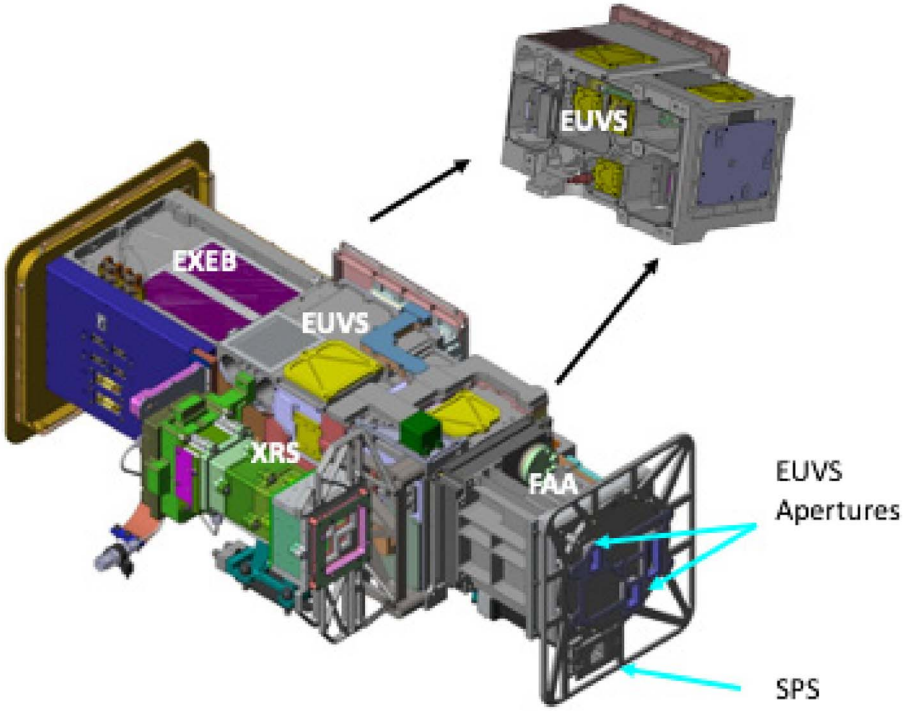


**Figure 6.** The EXIS instrument consists of four modules: XRS, EUVS, EXEB, and FAA. EUVS-C is one of three spectroscopic subsystems within the EUVS.

- Whereas the GOES remote sensing instruments that image the earth are nadir pointed, those that view the sun (EXIS, the Solar Ultraviolet Imager (SUVI), and the Compact Coronagraph-1 (CCOR-1) for the GOES-R series are mounted on a Sun Pointing Platform (SPP), which is attached to the yoke of the spacecraft solar array. In this configuration, EXIS, SUVI, and CORR-1 can view the sun throughout the entire day except for short periods of time, up to a maximum of approximately 72 min, that occur during two eclipse periods each year (February 26 – April 12 and August 31 – October 16). SPP mounting drove EXIS mass and volume requirements, which were accommodated with a modular design in which all the spectrographic channels were implemented as modules within a single EUVS housing (Figs. 6 and 7). In addition, it placed a >40 arc minute field of view (FOV) requirement on all measurements.

## 3 Instrument description

### 3.1 Instrument overview

EXIS instrument design is modular with four components (Fig. 6) consisting of an X-ray Sensor (XRS), an Extreme Ultraviolet Sensor (EUVS), an EXIS Electrical Box (EXEB), and a Front Aperture Assembly (FAA), which also includes a visible-light quadrant-photodiode Solar Position Sensor (SPS) that reports the location of the solar disk within the instrument FOV. A rotary door and filter wheel are also housed at either end of the FAA. EUVS consists of three spectroscopic channels (A, B, and C) covering eight discrete bands in the 25 nm – 280 nm spectral range.

Figure 7 is an exploded view of EUVS. It consists of a single-piece instrument case into which subassemblies of the three channels are mounted using o-ring gaskets to seal against

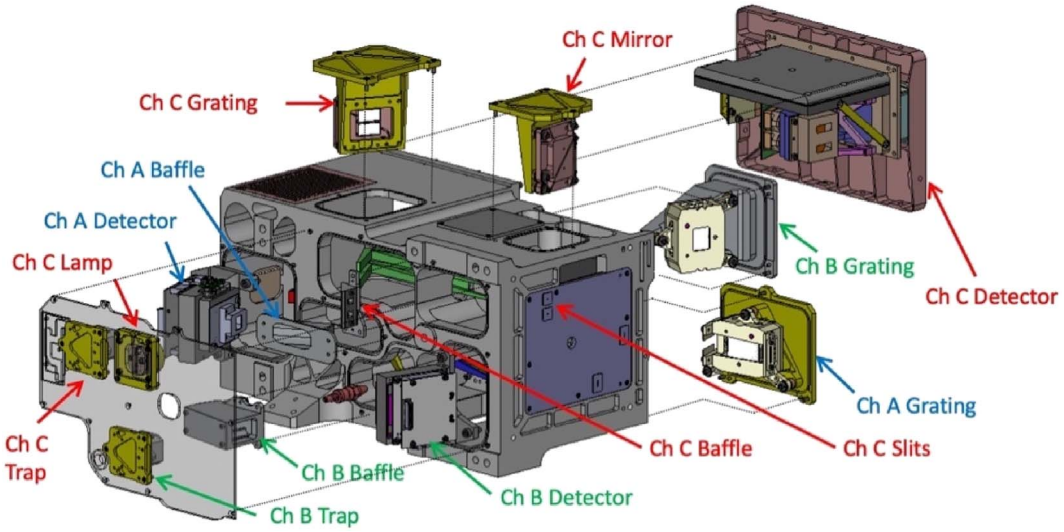


**Figure 7.** EUVS exploded view showing the major subassemblies for each of the three channels.

light leaks. EUVS-A, which covers three discrete bands centered at 25.6 nm (He II), 28.4 nm (Fe XV), and 30.4 nm (He II), and EUVS-B, which covers four discrete bands at 117.5 nm (C III), 121.6 nm (H Lyman alpha), 133.5 (C II) and 140.5 (Si IV, O IV), are single-bounce optical systems. They employ grazing incidence (A) and normal incidence (B) concave gratings to image their spectra onto 24-element photodiode arrays equipped with custom application-specific integrated circuit (ASIC) readouts (Aalami & Jones, 2009). EUVS-C is a pair of identical two-bounce optical channels employing concave gratings and toroidal imaging mirrors to project their spectra onto 512-element n-channel metal- oxide-semiconductor (NMOS) self-scanning diode arrays. All channels include traps for light diffracted from their gratings into zero-order and baffles to eliminate glints from the apertures in the EXIS FAA. Each EUVS-C channel is equipped with a thermal control subsystem that maintains the detector temperature at approximately −10 °C. EUVS-A and EUVS-B operate at the nominal EUVS case temperature. Each EUVS-C channel also includes an auxiliary optical system that directs light from an internal UVTOP280 285-nm emitting diode into its main optical path by reflecting it from the back side of the spectrograph entrance slit. This is used as a "flat field" lamp that tracks the relative response of the detector pixels. The EUVS-A and -B channels also have UVTOP280 flat field lamps, but these are mounted inside their respective detector housings to provide direct detector illumination.

### 3.2 EUVS-C detector and optical system design

EUVS-C consists of two identical optical-detector chains referred to as C1 and C2. Figure 8 is a cross-section view through the EUVS case in the EUVS-C dispersion plane with the optical path for a single channel shown in green. Each EUVS-C optical-detector chain employs a S3904-512Q Hamamatsu NMOS linear array detector. The EXIS FAA, which is attached to the front of the EVUS (Fig. 6) includes a door and a filter wheel with mechanical covers that block unwanted light from entering the EUVS-C. Either C1 or C2

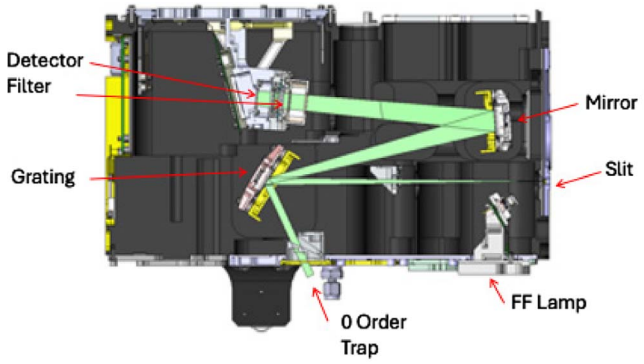


**Figure 8.** A cross-section view of the EUV in the dispersion plane of EUVS-C. The optical path, including the zero-order from the diffraction grating, is shaded in green.

or both C1 and C2 can be illuminated by the sun through apertures in these mechanisms, but no filter wheel position simultaneously blocks both C1 and C2. During nominal operations, only one channel is illuminated. The other is held as a backup. The door, which is opened once in orbit after instrument commissioning, protects EXIS during ground operations and launch.

CMOS technology was chosen for the EUVS-C because it is more radiation tolerant than that of CCD-based detectors. In addition, CMOS has a one-dimensional implementation that is ideal for spectroscopic applications similar to EUVS-C, for which no spatial imaging along the spectrograph entrance silt is required. The Hamamatsu S3904-512Q NMOS detector was selected for EUVS-C. It consists of a 398 μm thick P-type silicon substrate with a 512-element array of 1.0 μm thick × 20 μm wide × 2.5 mm tall N-type structures, spaced at 25 μm, imbedded in its top surface, providing a pixel response function that is trapezoidal with a 25 μm FWHM and a 30 μm base width. A nominally 1.0 μm thick passivation layer of $SiO_2$ covers the top surface. The pixel-to-pixel response nonuniformity is <0.5% across the entire array.

S3904 devices have a nominal 3500 electrons ($e^-$) read noise due to the relatively large pixel area (100 times that of a typical CCD with 25 μm square pixels) and have a typical 24 picocoulomb (pC) output saturation charge equivalent to $1.5 \times 10^8$ electrons ($e^-$). The photon transfer function (change in detector output for change in incident photon flux) is linear up to better than 90% of capacity. EUVS-C readout electronics have an electron gain of $1.5 \times 10^3$ $e^-$ per data number (DN) and a 16-bit output register, resulting in an electronics output saturation of 15.5 pC, which is ~62% of the detector's full well. Nominal detector dark @25 °C is 0.1 picoamps (pA) that varies as a function of temperature ($T$): $I_{\mathrm{Dark}}(T) = I_{\mathrm{Dark}}(T_0)\cdot e^{0.14\cdot(T-T_0)}$. Flight detector temperatures are maintained at ~ −10 °C by a thermal control system (see below) resulting in a nominal beginning of life dark currents of 0.75 femtoamps (fA). Because NMOS detector dark current increases with exposure to energetic particles and ionizing radiation, there is a mission-level requirement that limits EUVS-C detector radiation exposure to <15 krad over the 15-year mission lifetime. This is met using a combination of aluminum and tungsten shielding around each detector that limits lifetime exposure to 2.2 krad. Dark current in engineering model detectors increased by a factor of 4 after an 8.8 krad exposure to 150 MeV protons at the Indiana University Cyclotron Facility (Pollock, 1977). Dark current levels in the EUVS-C flight detectors are measured in real-time using outputs from pixels at one end of the array that is shielded from incoming solar photons by an opaque mask.

In EUVS-C operation, the *P-N* junction of each pixel in the array is sequentially reversed-biased by momentarily connecting it to a fixed preamplifier voltage source at the beginning of an integration period. As photons enter the junction region, a fraction of them is absorbed, promoting electrons to the conduction band of the semiconductor. These flow to the junction, reducing the bias voltage. Thermal electrons within the substrate (dark current) also flow into the junction, which additionally reduces the bias voltage. At the end of the integration period, the array is readout at a rate of 40 μs per pixel (0.02048 s for the entire array) by sequentially reconnecting each one to the preamplifier where accumulated charge is converted to a voltage that is then digitized in an analog-to-digital converter. This operation also returns the pixel to the reverse-biased state for the next integration. In the EUVS-C implementation, the detector is synchronized to the instrument clock, and the readout begins at a quarter-second tick and requires 0.02048 s to execute. This is followed by a short integration ("dead" time), which is programmable in increments of 0.025 s. Then the array readout is repeated two more times. These additional read cycles "flush" the diodes minimizing lag, which is an incomplete pixel reset, that is a characteristic of CMOS detectors. Once the second flush of a pixel occurs, its new integration cycle begins. A cycle terminated with the initiation of a subsequent readout after N quarter sec clock ticks. EUVS-C integration cycles are commanded by the EXIS Electrical Box and can be varied in 0.25 s increments starting at 0.25-second by uplinked ground commands to the instrument.

The S3904-512Q's pixel configuration, dark current characteristics, and radiometric performance are key drivers of the EUVS-C optical implementation. Assuming the first 60 pixels of the detector array are reserved for dark current measurement, the requirement for 275–284.5 nm wavelength coverage across 450 elements with ~5 samples per 0.1 nm resolution element sets an optical performance requirement that the image formed at the detector focal plane by the convolution entrance slit width and the optical line spread function be ~0.125 mm FWHM. The required spectral dispersion is ~0.85 nm/mm.

Table 2 summarizes the EUVS-C optical design parameters imposed by the detector choice. It is a modification of the single-concave-grating Rowland circle mount suggested by Snow & McClintock (2005). Adding a toroidal concave mirror both shortened the original 300 mm focal length design by 85 mm and provided additional optical surfaces to control image aberration.

Sunlight enters the EUVS-C through a 0.1 mm wide × 0.5 mm tall rectangular slit and impinges on a concave grating that diffracts first-order wavelengths centered at 280 nm toward an imaging mirror. Light leaving the mirror passes through a bandpass filter before being imaged on the detector. The combined system produces a spectrum centered at 280 nm with an average wavelength dispersion of 0.84 nm/mm and a diffraction-grating anamorphic magnification of $(\cos(\alpha))/(\cos(\beta) = 1.25)$.

The EUVS-C gratings are replicas of a master fabricated by Jobin Yvon (JY) onto 10.16 × 18.29 mm rectangular substrates with a ruled area of 9 mm tall × 12 mm wide. This provides an ~2° FOV that exceeds the > 40 arc minute FOV requirement imposed to accommodate EXIS on the spacecraft SPP. The grating has a 464.55 mm radius of curvature and a 4549.4 grooves per mm ruling density. Its groove profiles are pseudo-sinusoidal with a depth of 60 nm and a 0.55 valley-to-spacing ratio. This configuration suppresses light, leaving the grating in even diffraction orders, and provides an absolute efficiency of 50% for unpolarized light across the EUVS-C's 275–284.5 nm wavelength range.

The imaging mirror has a 12.4 mm tall × 21.6 mm wide aperture and a concave toroidal figure with radii of curvature 340.6 mm (dispersion plane) and 297.5 mm, respectively. The smaller radius reduces the height of the final astigmatic image height over the field from 2 mm to 0.2 mm, relaxing detector alignment tolerances. Both the grating and mirror substrates are ultralow expansion (ULE) quartz coated with unprotected aluminum. This provides high reflectance ($R$ ~ 0.9) and avoids any issues that might arise from radiation damage in protective dielectric overcoats.

An interference filter and long-wavelength blocking filter pair are located 10 mm in front of the detector. These consist of two 1 mm thick substrates, spaced 1 mm apart and oriented parallel to the detector input surface. The first element contains an interference filter, and the second is a long wavelength blocking filter. This combination is designed to provide adequate transmission for the 275–284.5 nm wavelength range while strongly attenuating the $\lambda > 295$ nm sunlight that enters the entrance slit (blocking to better than $10^{-6}$ for $295 < \lambda < 825$ nm and better than $10^{-5}$ for $825 < \lambda < 1100$ nm). Barr Associates designed and fabricated the filter, which closely resembles the one used in the Cloud Imaging and Particle Size Instrument aboard the Aeronomy of Ice in the Mesosphere spacecraft (McClintock et al., 2009). The Hamamatsu detector package includes a custom fused silica window located 1.3 mm in front of the NMOS input face. One end is aluminized in order to block the spectral image from reaching approximately 60 pixels located at the short-wavelength end of the

**Table 2.** EUVS-C optical elements and geometry.

| Element | Parameters | Comments |
|---|---|---|
| Entrance slit | 0.1 mm × 0.5 mm | Slit – grating separation: 200.0 mm |
| Grating | 464.55 mm | Incidence angle: $\alpha$ = 32.6° |
| Radius of curvature | 4549.4 g/mm | Diffraction angle: $\beta$ = 47.5° |
| Ruling density | | Grating – mirror separation: 169.9 mm |
| Mirror | 340.6, 297.5 mm | Incidence angle: 10.0° |
| Radii of curvature | | Mirror – filter separation: 179.1 mm |
| Filter | 1 mm | Two 1 mm thick substrates one carrying a 18 nm wide bandpass filter and the other a 0.29 – 1.1 mm blocking filter |
| Substrate thickness | | Filter – detector separation: 10 mm |
| Detector | 512 × 1 | Custom anti-reflection coated window blocks light for 60 diodes for dark current monitoring 24 pC ~1.5 × $10^8$ $e^-$ |
| Format | 0.025 × 2.5 mm | |
| Pixel size | 24 pC | |
| Charge capacity | 1500 $e^-$ per DN | |
| Gain | 3500 $e^-$ | |
| Read noise | 6.25 × $10^5$ $e^-$/s | |
| Dark current | 4.65 × $10^3$ $e^-$/s | |
| @+25 °C | | |
| @−10 °C | | |

array, resulting in a final 275.1 nm – 284.6 nm design spectral coverage. These blocked pixels act as a real-time monitor of dark current plus particle backgrounds plus electrical offset (Sect. 5.2). The entire window has an anti-reflection (AR) coating provided by Barr Associates. Spare interference-blocking filters and windows from the flight deliveries were tested to 10.5 krad for radiation damage with no observable shift of in-band wavelength or loss of transmission.

The scattered light is controlled by the combination of filter blocking and the grating scattered light profile that was specified (but not measured) as 2 × $10^{-4}$/nm. Light with wavelengths < 350 nm is diffracted by the grating and reflected by the imaging mirror toward the focal plane. Wavelengths > 350 nm are diffracted through angles that are too large for them to intersect the mirror and impinge upon the spectrograph housing where they scatter diffusely. Scattered light analysis, performed using Zemax, predicted that the detector output from each pixel resulting from these sources would be ~200 $e^-$/s.

Figure 9 is a cross-section view of the detector assembly and an exploded view of the detector-filter mounts. The assembly is designed as a complete module that is inserted in the EUVS housing as a unit and provides the mechanical mounting for the detectors and their readout electronics in the two optical chains' focal planes. In addition, it performs three key functions: optical shielding from out-of-band light, mechanical shielding from high energy gamma-ray photons produced in the EUVS housing by deceleration of energetic electrons, and thermal control. The inset in Figure 9 is an exploded view of the detector-interference filter assembly. It consists of a tungsten housing into which the detector is inserted, followed by a mask that acts as an optical field stop, exposing only the 12.8 mm wide × 2.5 mm tall active area to incident photons. The filter assembly is mounted directly to the detector housing. This arrangement provides shielding from gamma ray photons produced as high energy electrons decelerate within the EXIS instrument structures. It also provides a light-tight enclosure for the detector that prevents stray visible light that enters the EUVS-C entrance slit from reaching the detector. The detector assembly also includes a thermal control subsystem consisting of an external radiator and heaters. It is attached to a detector subassembly, which consists of the housing, readout electronics, and additional tungsten shields, with a mechanical interface that acts as a heat strap. The radiator is large enough to cool the subassembly to −30 °C. Replacement heaters provide the power to maintain the subassembly at −10 °C under proportional-integral-differential (PID) control.

Two baffles, a zero-order light trap, and a detector field lamp, are also included in each EUVS-C optical system. The first baffle, which is located ~100 mm behind the entrance slit, contains a mask and is designed to prevent glints from structures within the FAA from reaching the grating. A second baffle blocks direct light paths from the entrance slit to the detector. Light reflected from the grating in zero-order (angle of diffraction equals the angle of incidence) is directed toward an EUVS enclosure wall, where it enters a trap consisting of the black-coated wedge that absorbs >99% of the incident light.

### 3.3 Imaging and radiometric performance

Imaging performance was evaluated using Zemax raytrace software. System line-spread-function (LSF) results are summarized in Figure 10 for the center of the field of view (offset by 0.05 for clarity) and for SPP offsets of 0.5° and 0.5° in azimuth and elevation, respectively. They include the convolution of the imaging system and the detector LSFs and are shown for six wavelengths between 275 nm and 285 nm. The primary image defects encountered at off-axis azimuth field angles are stretch and shift in the wavelength scales. FWHM of these profiles is ~ 0.10 nm.

$R(\lambda_j)$, the instrument responsivity, is the product of the entrance slit area ($cm^2$), the reflectance of the mirror ($R_{Mirror}$ ~ 0.85 for all wavelengths), average diffraction efficiency for the grating *s* and *p* polarizations, the transmission of the filter, detector quantum efficiency ($e^-$/photon) and bandpass for a single pixel (~0.021 nm).

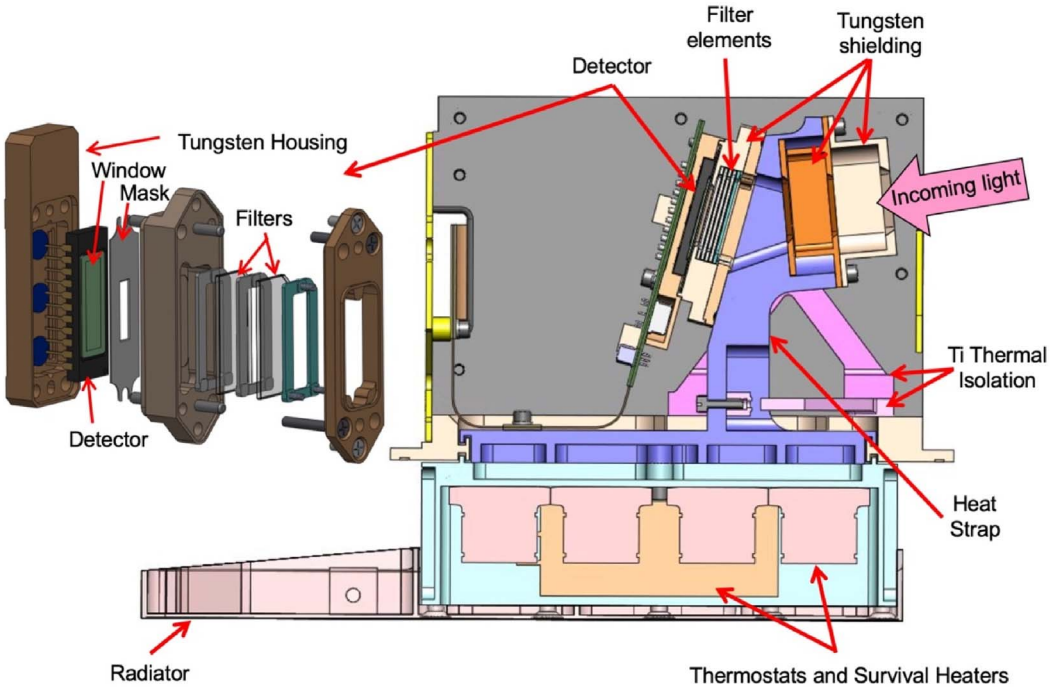


**Figure 9.** Detector assembly cross section and detector and filter mounting detail.

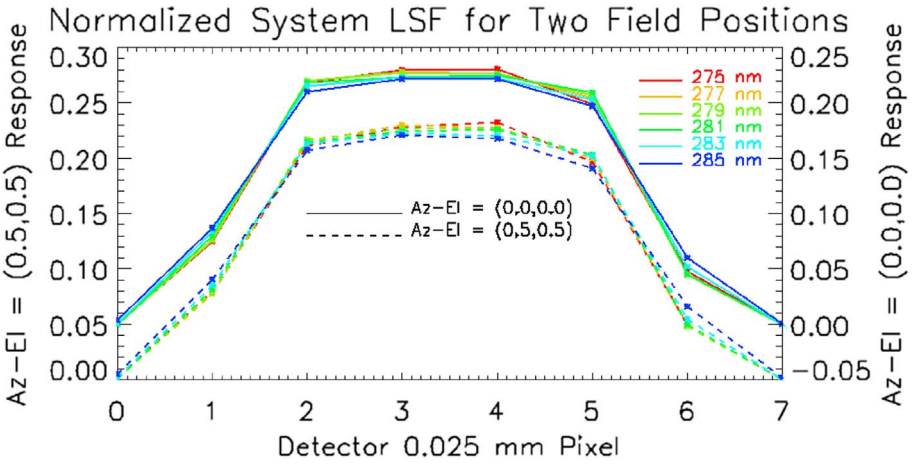


**Figure 10.** , EUVS-C line spread functions for six wavelengths at center FOV (sold). Dashed LSF for off-axis viewing angles are nearly identical (dashed). 10b, Spectral shift, and stretch are present for off-axis viewing angles.

Filter in-band transmission and detector quantum efficiency values, measured at the Laboratory for Atmospheric and Space Physics (LASP) at the University of Colorado, and modeled grating efficiencies provided by Jobin Yvon are plotted in Figure 11 along with the calculated values for $R(\lambda_j)$.

## 4 Instrument characterization and calibration

Calibration and characterization measurement of the EUVS-C in the assembled EXIS instrument were performed at LASP and at the National Institute for Standards and Technology's (NIST's) Synchrotron User's Radiation Facility III (SURF III, Arp et al., 2002). Measurements included imaging performance, wavelength scale determination, radiometric responsivity, field of view maps, dark current characterization, and scattered light.

### 4.1 Imaging and wavelength scale

PSF and wavelength scale were measured for each channel using LASP's EXIS Laser Facility (ELF) and Spectral Radiometer Facility (SRF, Richard et al., 2020), which produced F/100 monochromatic input beams to the instrument. Gaussian functions, fit to each profile within the FOV, consistently yielded 4-pixel-wide FWHM values, consistent with the system imaging models in Figure 7a. Wavelength positions, measured in air ($\lambda_{vac} = \lambda_{air} - \sim 0.08$ nm), were determined from

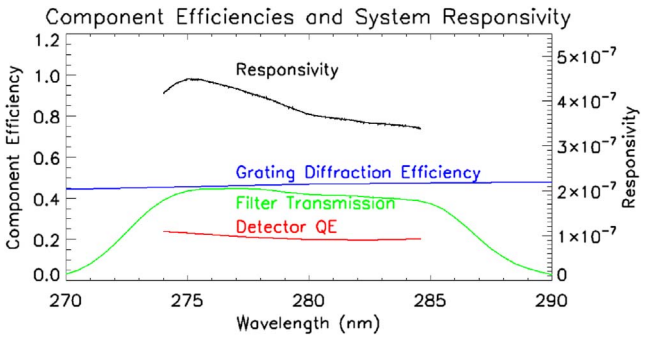


**Figure 11.** Component efficiencies (left axis) and predicted instrument responsivity, units = electron/(photon/cm2/nm) (right axis).

the centroids of the laser line images at the FOV center only. These were fit with a simple quadratic

$$\lambda_N = \lambda_0 + A_1 \cdot N + A_2 \cdot N^2, \quad (3)$$

where $N$ is the pixel number (0–511). Values of $A_1$ and $A_2$ ranged between 0.02175, 0.02151, 0.02078, and 0.02163 and $-1.59 \times 10^{-6}$, $-1.24 \times 10^{-6}$, $-1.40 \times 10^{-6}$, and $-1.36 \times 10^{-6}$ for GOES-16, GOES-17, GOES-18, and GOES-19 respectively, reflecting slight differences in channel-to-channel as-built focus. These are consistent with $A_1 = 0.020$ and $A_2 = -1.4 \times 10^{-6}$ determined from the ray trace model.

### 4.2 Radiometric responsivity

Determining the absolute radiometric responsivity at FOV center – $R(\lambda_j, \theta = 0, \phi = 0)$ – in equation (7) was the primary SURF measurement. It was performed using Beam Line 2, which is equipped with a large vacuum tank containing a mechanical manipulator consisting of a platform with two axes of spatial motion perpendicular to the photon beam ($x$-$y$) and a gimbal with two axes of angular motion (azimuth-elevation). The center line of the gimbal is located 17.8244 m from the tangent point of the synchrotron storage ring, resulting in a nearly collimated beam (divergence angle ~ 0.07°) that is linearly polarized in the electron orbital plane (horizontal with respect to the room). This was accommodated by mounting EXIS in the manipulator with the grating grooves in the EUVS channels oriented at $\theta = 45°$ with respect to the room vertical (and to the orbital plane). In addition, the plane containing the EUVS entrance slits was located on the rotation axes of the gimbal to eliminate beam displacement during field-of-view mapping. Responsivities ($e^-$/(photon/cm$^2$/nm)) for the GOES-16 and GOES-17 C2 Channels and the GOES-18 and GOES-19 C1 Channels are plotted for $\theta = -45°$ and a detector temperature of $T = -10$ °C in Figure 12 along with the estimated component-level responsivity from Figure 11. Identical results were measured for $T = -10$ °C and $\theta = +45°$ and for $T$ from −15 °C to +5 °C in 5° steps for both angles. Absolute uncertainties in the SURF measurements are estimated to be approximately 5%. These results largely due to the uncertainties associated with repeatably placing the center of EUVS-C in the center of the SURF beam. Differences in the curves seen in Figure 12 are real differences in the responsivities rather than measurement noise.

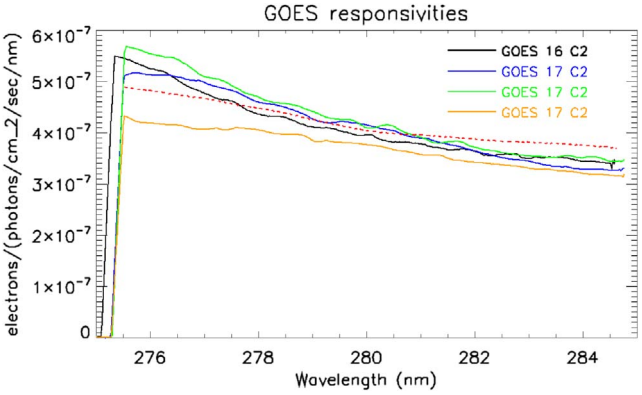


**Figure 12.** GOES-16 C2, GOES-17 C2, GOES-18 C1, and GOES-18 responsivities are plotted in black, blue, green, and orange, respectively. These were selected as the operational channels at spacecraft commissioning. The red dashed curve is the estimated sensitivity computed from component-level efficiency measurements (Fig. 11).

### 4.3 Field of view response

Relative responsivity as a function of FOV ($F(\theta, \phi)$ in equation (6) was measured at both SURF and at LASP using the ELF/SUR. Whereas cruciform alignment scans at SURF measured only along the instrument axes, raster scans performed at LASP covered a 2° wide square FOV in 0.25° steps (half the solar diameter). The contour map of the GOES-17 $F(\theta, \phi)$ shown in Figure 13 is a typical example. It was made with the LED source and F/100 beam after binning six spectral pixels centered at a $\lambda = 280$ nm to simulate the integration over the $k$ and $h$ line emission cores. Maps at 276 nm and 284 nm vary from those at 280 nm by < ±1%. Maps for GOES-16, GOES-18, and GOES-19 give similar results, with the responsivity varying by ±3% or less over the 2° FOV.

Whereas the F/100 beam closely simulates the solar disk, the F/1000 beam more precisely probes the pixel-to-pixel response. Figure 14 shows spectra of a laboratory UVTOP – 280 LED taken in the LASP ELF facility using an F/1000 input beam to map the response of GOES-17 EUVS-C response in a ± 1° angular range in the cross-dispersion direction. The spectra at each step were normalized to 1 at the peak and sequentially offset by 0.04 units for clarity. Three regions, plotted in blue, show local depressions that are ~5% deep and span 5–10 pixels. These features were also detected in scans using an F/100 input beam but their depths were reduced by a factor of ~6. Their origin was traced to imperfections in the interference filters that are located ~35 mm in front of the detectors. The area of the F/1000 beam at the filter is ~ 0.04 mm$^2$; thus, 5% depression in responsivity suggests that there is a 100% opaque circular obstruction with a diameter of 0.05 mm. When probed with an F/1000 all EUVS-Cs exhibit these features in about the same numbers. The impact of these artifacts on the flight data is discussed by McClintock et al. (2025).

### 4.4 Detector dark current, read noise, and electrical offset

$D_{\text{Dark}}$ and $D_{\text{Offset}}$ are the detector's dark current output and electrical offset, measured in data numbers (DN). These were

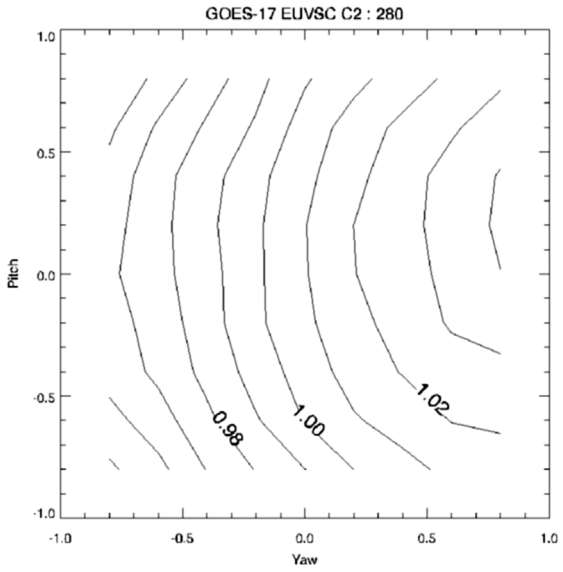


**Figure 13.** left: GOES-17 EUVSC field of view responses for 280 nm.

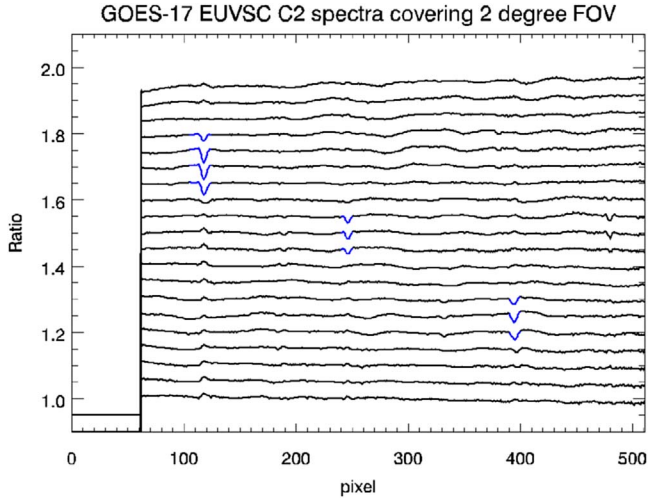


**Figure 14.** Twenty individual spectra taken at 0.1° step intervals along a 2° scan perpendicular to the instrument dispersion direction. They have been normalized to 1 at their peaks and offset by 0.04 units for clarity. Three regions plotted in blue mark locations with reduced sensitivity. These are likely caused by blemishes in the interference filter located in front of the detector.

characterized using SURF data obtained for integration times ranging from 0.25 to 64 seconds at the nominal −9.5 °C flight operating temperature and for five additional detector temperatures, ranging from −17.1 °C to +7.2 °C at a single 5-second integration time. The former measurements were used to determine dark current rates for the detectors in EUVS-C that operate at a nominal temperature of −9.5 °C. Average values for the eight detectors at this temperature were in the range of 2.62–2.72 DN/pixel/s with pixel-to-pixel variations within individual detectors of ~0.1 DN/pixel/s or less. These extrapolate to 328–341 DN/pixel/s = ~0.08 picocoulombs/pixel for a temperature of 25 °C, which is consistent with the Hamamatsu's 0.1 picocoulombs nominal performance estimate and also consistent with detector unit level measurements made at LASP. Dark current shot noise at −9.5 °C, which is ~ 0.04 * $\sqrt{t_{int}}$ DN, where $t_{int}$ is the integration time in seconds, makes a negligible contribution to the determination of $D_{Dark}$. Read noise values, extrapolated from the dark current measurements, were ~3500 $e^-$ (2.33 DN).

The measurements over −17.1 °C to +7.2 °C showed that $D_{Offset}$ can be represented as $D_{Offset} = D_{Offset\text{-}Elect} + D_{Offset\text{-}Pixel}$. $D_{Offset\text{-}Elect}$ is a constant term for all pixels that arise from an electrical offset applied to the detector charge-to-voltage conversion amplifier. The pixel-to-pixel structure, $D_{Offset\text{-}Pixel}$, which arises from variations in the individual pixel + video line capacitance within the detector and has a pronounced odd-even effect, has a typical amplitude ±5 DN amplitude across the entire array.

### 4.5 Stray and scattered light

Out-of-band stray and scattered light were measured for $\lambda > 350$ nm at LASP using a heliostat to illuminate EXIS. There was no evidence for stray and/or scattered light signals above the dark current to better than 0.5 DN observed in these measurements. This also verified that the EUVS-C detector enclosures are light tight. During instrument definition, the contribution to scattered light for $\lambda < 350$ nm was modeled. Those calculations showed that as a result of relatively weak solar irradiance below 350 nm, low detector sensitivity, and good filter blocking, the contribution from this wavelength range was less than 5% of the total scattered light. Thus, the scattered light term in radiometric calculations (e.g., Eq. (5) is set to 0).

## 5 Predicted flight performance

### 5.1 Spectral resolution

The red line in Figure 15 is a simulation of the anticipated spectral resolution performance obtained by convolving a 0.01 nm spectral resolution solar spectrum (black line) measured during balloon flights on April 19, 1978, and April 20, 1983 (Hall & Anderson 1988, 1991) with the 280 nm LSF shown in Figure 14 sampled at 0.02 nm per bin.

For comparison, a daily average SORCE-SOLSTICE spectrum taken on December 18, 2014, which is sampled at 0.025 nm per bin, is shown in blue. Both EUVS-C and SOLSTICE provide slightly better chromospheric-core to photospheric-wing isolation than a triangular 0.1 nm FWHM PSF (Fig. 4) but still mix in a photosphere component to the total chromosphere emission relative to the spectrum with 0.01 nm resolution.

### 5.2 Radiometric performance and precision

Equations (4)–(6) relate instrument optical and detector performance to solar irradiance:

$$D(j) = \left(S(j) - D(j)_{Offset}\right) \cdot FF(j) \cdot \mathrm{LIN}. \quad (4)$$

$D(j)$ is the raw detector output, $S(j)$, is corrected for electrical offset, flatfield, and linearity where $D_{Offset}$ is the electrical offset

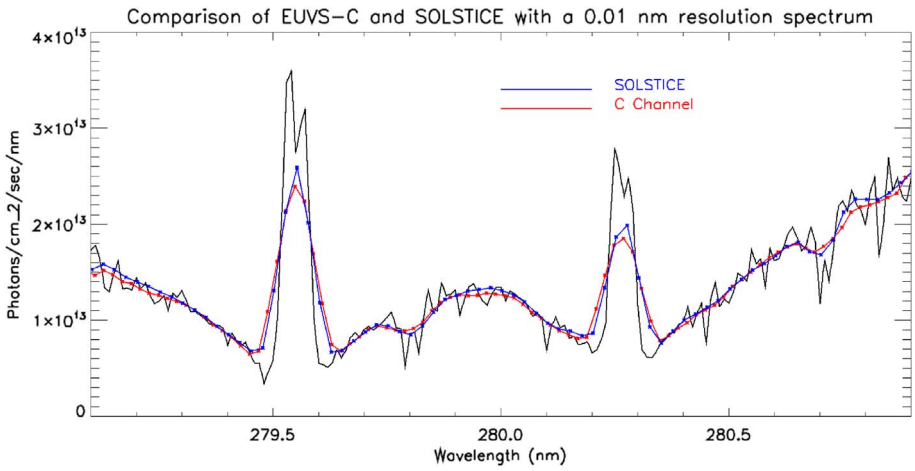


**Figure 15.** Comparison of a 0.01 nm spectral resolution solar spectrum observed from a balloon (black) with a spectrum observed with SORCE-SOLSTICE (blue) and with a simulated EUVS-C spectrum (red). The spectral resolution for SOLSTICE and EUVS-C is ~ 0.1 nm.

applied to the detector charge-to-voltage amplifier (Sect. 4.4), *FF* is a flatfield correction for pixel-to-pixel photoresponse nonuniformity, which is typically less than 0.5% across the entire array, and LIN is a correction that accounts for nonlinear effects in the detector photon transfer function. LIN = 1 for $S'(j) - D(j)_{\text{Offset}} < 9.0 \times 10^4$ DN. Then,

$$I(\lambda_j)_{\text{SUN}} = \frac{D(j) - D(j)_{\text{Dark}} - D(j)_{\text{Scatter}} - D(j)_{\text{Bkgd}}}{R(\lambda_j) \cdot G \cdot \Delta t} = \frac{D'(\lambda_j)}{R(\lambda_j, \theta, \phi) \cdot G \cdot \Delta t}, \quad (5)$$

$$R(\lambda_j, \theta, \phi) = W_{\text{Slit}} \cdot H_{\text{Slit}} \cdot R(\lambda_j)_{\text{Grat}} \cdot R(\lambda_j)_{\text{Mirror}} \cdot T(\lambda_j)_{\text{Filter}} \times QE(\lambda_j)_{\text{Detector}} \cdot \Delta\lambda(j) \cdot F(\lambda.\theta, \phi). \quad (6)$$

$I(\lambda_j)_{\text{SUN}}$ is the solar spectral irradiance at the wavelength $\lambda$ associated with pixel $j$, and $D_{\text{Dark}}$ is the data number output resulting from dark current within the detector. $D_{\text{Scatter}}$ is output resulting from stray and scattered light within the optical system that reaches the detector. This is set equal to 0 based on the optical analysis (Sect. 3.2) and calibration measurements (Sect. 4.5). $D_{Bkgd}$ is the output due to hits from energetic particles and gamma rays that penetrate the detector shields. The corrected DNs in the numerator of equation (4) are referred to as $D'(\lambda_j)$, the signal in pixel $j$. $R(\lambda_j)$ is the instrument responsivity, reported in electrons/(photons/cm$^2$/nm/s) (Fig. 12). Values for its components are plotted in Figure 8. The terms in equation (7) assume the instrument boresight is pointed directly at the sun. $F(\lambda,\theta,\varphi)$ is a correction factor whose value is close to 1 that accounts for small variations in component efficiencies when the sun is viewed from non-zero azimuth and elevation angles $\theta$ and $\varphi$, respectively. $G$ is readout electronics gain ($G$ = DN/1500 e$^-$), $\Delta\lambda(j)$ is the spectral width of pixel $j$, measured in nm, and $\Delta t$ is the integration time in seconds. If the slit area is measured in cm$^2$ then the units for $I(\lambda_j)_{\text{SUN}}$ are photons/cm$^2$/s/nm.

The SURF measurements were used to estimate the C Chanel solar irradiance signal, defined as the numerator in equation (4), $D'(\lambda_j) = I(\lambda_j)_{\text{SUN}} \cdot R(\lambda_j) \cdot G \cdot \Delta t$ using SOLSTICE irradiance measurements and assuming $\Delta t$ = 3.0 s. This produces a maximum detector output of ~5 × 10$^4$ DN relative to the detector analog-to-digital converter's 65,535 DN full scale. The results are shown on the left side of Figure 16. On average, the signal levels in the wings are ordered 2 × 10$^4$ DN = 3 × 10$^7$ e− per 0.0215 nm pixel. Those in the emission cores are a factor of 3 – 4 smaller.

Suppressing the index $j$, the uncertainty in $I_{\text{SUN}}$ follows from equation (4)

$$\sigma^2_{I_{\text{SUN}}} = \frac{\sigma^2_{D'}}{R^2 \cdot G^2 \cdot \Delta t^2} + I^2_{\text{SUN}} \cdot \frac{\sigma^2_R}{R^2} + {I_{\text{SUN}}}^2 \cdot \frac{\sigma^2_G}{G^2} + I^2_{\text{SUN}} \cdot \frac{\sigma^2_{\Delta t}}{\Delta t^2}. \quad (7)$$

Whereas the numerator of the first term in equation (7) contains random errors that directly impact precision, the last three terms are systematic errors that affect the accuracy in $I_{\text{SUN}}$ but not the precision. Expanding the first term numerator and deleting the terms with only systematic components (FF, Lin, and Offset) and setting $D_{\text{Scatter}}$ = 0 yields the random errors in irradiance

$$\sigma^2_{D'} = \sigma^2_D + \sigma^2_{D_{\text{Dark}}} + \sigma^2_{D_{\text{Bkgd}}}. \quad (8)$$

In the first term of equation (8), random errors in the detection of photon and background events and the production of event electrons within the detector pixels are described by a Poisson probability distribution. If $N$ is the number of event electrons (the sum of signal + dark + scatter + background), then the uncertainty, which is often referred to as shot noise, is $\sqrt{N}$, and the precision of that measurement is signal shot noise/signal = $1/\sqrt{N}$. The corresponding signal and uncertainty in DN are $G \cdot N$ and $G \cdot \sqrt{N}$. For EUVS-C, $G$ = 1/1500 DN per electron. Conversion from event electrons captured in a detector pixel to output data numbers introduces two additional uncertainty terms in $\sigma_{\text{D}}$. The first is detector read noise ($\sigma_{\text{Readnoise}} \sim \pm 3500\,\text{e}^- = \pm 2.33$ DN per pixel) and the second is digitization noise that arises from the electron-to-data number conversion ($\sigma_{\text{Digit}} = \pm\frac{G}{\sqrt{12}} \sim \pm 430\,\text{e}^- = 0.29$ D per pixel). Combining these leads to

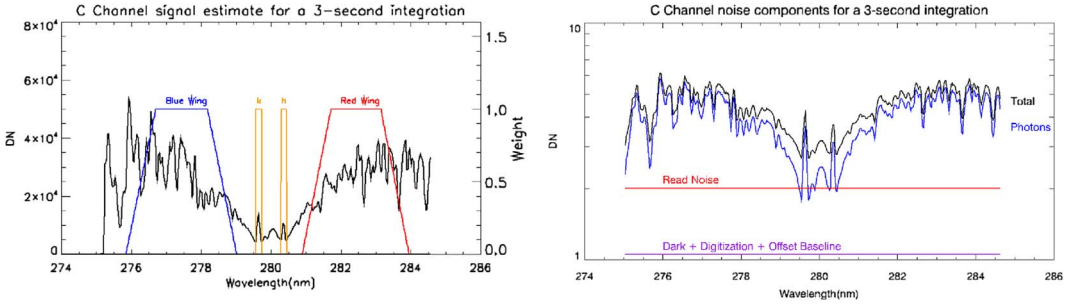


**Figure 16.** On average the signal levels in the wings are on order $2 \times 10^4$ DN = $3 \times 10^7$ $e^-$ per 0.0215 nm pixel. Those in the emission cores are a factor of 3–4 smaller. Figure 16 Left: GOES-16 estimated signal for a 3-second integration using SURF calibration measurements. Weighting functions used to calculate $MgII_{EXIS}$ (Sect. 5.3) are superimposed on the spectrum. Right: Noise contributions for a 3-second integration. Solid lines represent random components. The ±1DN uncertainty in the sum dark current + detector offset is dashed. Negligibly small random terms arising from particle backgrounds and scattered light are not shown.

$$\sigma_D^2 = [D \cdot G + 5.53]. \tag{9}$$

Two sources contribute to random variations in the second term in equation (8), detector dark signal, $\sigma^2_{D_{\text{Dark}}} = \sigma^2_{DS} + \sigma^2_{DT}$. The first of these is dark current shot noise. EUVS-C temperatures are actively maintained at −10° ± 1 °C, resulting in a per-pixel dark current of $4.65 \times 10^3$ $e^-$/s and a shot noise of $\sigma_{DS} \sim 120$ $e^-$ for a 3-second integration. The second, more significant, source of dark current fluctuations is caused by instabilities in detector temperature. Dark current varies by ±15% for temperature changes of ±1°, and the dark charge collected in a single pixel during a 3-second integration varies by $\sigma_{DT} \sim \pm 2100$ $e^-$ for a nominal −10 °C temperature. This is a factor of ~15 greater than the shot noise. Estimates of on-orbit detector radiation damage indicate that these values may increase by a factor of 4 by the end of life (EOL). In addition, whereas shot noise (both photon and dark) is independent from pixel-to-pixel, temperature-induced fluctuations are correlated, and the uncertainty introduced into the sum of $N$ pixels is $\sum_N \sigma^2_{DT} = N^2 \cdot \sigma^2_{DT}$ compared to $\sum_N \sigma^2_{DS} = N \cdot \sigma^2_{DS}$ for shot noise. Rather than implement requirements for strict temperature control and knowledge, dark current uncertainty was significantly reduced by masking 60 pixels on the short wavelength side of each channel and ensuring their output during each 3-second integration. This provides a real time monitor of $D_{\text{Dark}}$+$D_{\text{Offset}}$ that is accurate to ± 1 DN. The ratio of dark current in the masked pixels to that of the remaining pixels is measured weekly on orbit.

The geostationary environment is populated with energetic electrons and trapped solar protons (energies up to 10 MeV and 100 MeV, respectively). The detectors are protected from these particles by shields consisting 6 mm of aluminum. As particles decelerate within the shields, they produce Bremsstrahlung radiation, which is attenuated by an additional 2 mm of tungsten around the detector. Particle fluxes in geostationary orbit vary by a factor of 10 (10th to 90th percentile). The median flux of gamma rays reaching the detectors is 50 $cm^{-2}$ $s^{-1}$, increasing to 250 $cm^{-2}$ $s^{-1}$ at the 90th percentile. Assuming a single gamma produces 2 femto Coulombs (12500 $e^-$) that are deposited over a ~0.03 mm path length within the detector, the charge will typically be distributed over two pixels. On average, a pixel $6.4 \times 10^{-4}$ $cm^2$ pixel would encounter 0.064 events/s with 6250 $e^-$/event for median background levels. On average, each pixel produces ~ 400 $e^-$/s with a large variance. The deposition rate would increase by ~ 5X on the highest background days. The average signal from these events is ~ 0.8DN, which would easily be detected in the presence of 2DN read noise.

The right panel of Figure 16 summarizes the noise components in a measurement of $I(\lambda_j)_{SUN}$.

### 5.3 GOES index definition and precision

In addition to providing the required spectral resolution performance, EUVS-C is designed to measure the Mg II index ($MgII_{EXIS}$) with 0.1% precision or better. The GOES operational index (Snow et al., 2018), which is similar to that for SOLSTICE (Eq. (2)), is designed to produce near-real-time data with ~ 30-second latency using weighted sums of corrected signals, $D'(\lambda_j)$, rather than irradiance values, $I(\lambda_j)_{SUN}$

$$\text{MgII}_{\text{EXIS}} = \frac{D''_h + D''_k}{D''_{\text{BlueWing}} + D''_{\text{RedWing}}}, \tag{10}$$

where the terms in the numerator and denominator are weighted sums of corrected pixel values

$$D''_X = \frac{\sum_i \text{D}'_i \cdot W_{X,i}}{\sum_i W_{X,i}}, \tag{11}$$

$$\sigma^2_{D_x} = \frac{\sum_i \sigma^2_{D'_i} \cdot W^2_{X,i}}{[\sum_i W_{X,i}]^2} \tag{12}$$

with $x$ = BlueWing, RedWing, $h$ and $k$. Weighting functions for the wings are trapezoids with FWHM = 110 pixels and rectangles with $W$ = 9 and 8 for $k$ and $h$, respectively. These are superimposed on the spectrum in Figure 16a. Whether the separation of the current wing locations relative to $h$ and $k$ should be increased to avoid possible contamination by solar activity is under investigation.

The precision in the GOES index is calculated using a standard relationship for the uncertainty in the ratio of two independent variables (Bevington & Robinson, 2003),

$$\frac{\sigma^2_{A/B}}{(A/B)^2} = \frac{\sigma^2_A}{A^2} + \frac{\sigma^2_B}{B^2}, \tag{13}$$

where $A = D''_h + D''_k$ and $B = D''_{\text{BlueWing}} + D''_{\text{RedWing}}$ and $\sigma^2_{D''_x+D''_y} = \sigma^2_{D''_x} + \sigma^2_{D''_y}$.

Assuming that LIN = FF =1 and that $D_{\text{Scatter}} = D_{\text{Bkgd}} = 0$, evaluation of equation (10) using the signal levels in Figure 13a leads to $B = 5.5583 \times 10^4$ DN, $A = 1.6226 \times 10^4$ DN and $\text{MgII}_{\text{EXIS}} = 0.2919$. Precision follows from equation (12) with $\sigma_A = 1.631$ DN and $\sigma_B = 0.627$ DN: $\sigma_{\text{MgIIEXIS}}/\ \text{MgII}_{\text{EXIS}} = 1.01 \times 10^{-4}$, which is a factor of 10 better than the requirement.

## 6 Summary

The objective of the EUVS-C of the Extreme Ultraviolet Irradiance Sensor Aboard the NOAA GOES R Series Spacecraft is to make high precision (one part in a thousand), high time-cadence (3 s) measurements of the Mg II Index of Solar Activity. EUVS-C employs a concave grating spectrograph coupled with an NMOS linear sensor to record solar irradiance in the 275–285 nm wavelength range with spectral sampling and resolution (FWHM) of 0.021 nm and 0.10 nm, respectively, which enables separation of chromosphere Mg II emission from the surrounding continuum.

EUVS-C design and anticipated measurement performance are described here, along with results from preflight calibrations. These indicate that EUVS-C will meet its objectives for spectral resolution and cadence and has the radiometric performance necessary to exceed its precision objective by a factor of 10.

### Acknowledgements

Many researchers contributed indirectly to this work. They include the GOES-R EXIS team at the Laboratory of Atmospheric and Space Physics at the University of Colorado Boulder, the Synchrotron Ultraviolet Radiation Facility team at the National Institute of Standards and Technology, where the EXIS-C flight instruments were calibrated, and staff at the Cooperative Institute for Research in Environmental Sciences at the University of Colorado / NOAA NCEI who have contributed to understanding to their flight measurement performance. This research is supported by NASA Contract NNG07HW00C. The editor thanks two anonymous reviewers for their assistance in evaluating this paper.

### References

Aalami, DD, Jones AR. 2009. A low-noise ASIC electrometer for precision low-current measurements. *Proc SPIE* **7438**: 743816. https://doi.org/10.1117/12.826445.

Arp, U, Clark C, Farrell A, Fein E, Furst M, Hagley E. 2002. Synchrotron ultraviolet radiation facility SURF III. *Rev Scientific Instrum* **73 (3)**: 1674–1676. https://doi.org/10.1063/1.1445833.

Bevington, PR, Robinson DK. 2003. *Data reduction and error analysis for the physical sciences*. McGraw-Hill, United States. ISBN 0-07-247227-8.

Brueckner, GE, Edlow KL, Floyd LE, Lean JL, VanHoosier ME. 1993. The Solar Ultraviolet Spectral Irradiance Monitor (SUSIM) experiment on board the Upper Atmospheric Research Satellite, *J Geophys Res* **98**: 10695–10711. https://doi.org/10.1029/93JD00410.

Burrows, JP, Weber M, Buchwitz M, Rozonav V, Ladstatter-Weissenmayer A, et al. 1999. The Global Ozone Monitoring Experiment (GOME): mission concept and first scientific results. *J Atmos Sci* **56 (2)**: 151–175. https://doi.org/10.1175/1520-0469.

Chamberlin, PC, Eparvier FG, Knoer V, Leise H, Pankratz A, Snow M, Templeman B, Thiemann EMB, Woodraska DL, Woods TN. 2020. Flare Irradiance Spectral Model-Version 2 (FISM2). *Space Weather* **18 (12)**: e2020SW002588. https://doi.org/10.1029/2020SW002588.

Coddington, O, Lean JL, Pilewskie P, Snow M, Lindholm D. 2016. A solar irradiance climate data record. *Bull Am Meteorol Soc* **97 (7)**: 1265–1282. https://doi.org/10.1175/BAMS-D-14-00265.1.

Coddington, O, Lean J, Pilewskie P, Snow M, Richard E, et al. 2019. Solar irradiance variability: comparisons of models and measurements. *Earth Space Sci* **6 (12)**: 2525–2555. https://doi.org/10.1029/2019EA000693.

Deland, MT, Cebula RP. 1994. Comparison of the Mg II index products from the NOAA 9 and NOAA 11 SBUV/2 instruments. *Sol Phys* **152 (61)**: 61–68. https://doi.org/10.1007/BF01473184.

De Pontieu, B, Title AM, Lemen JR, Kushner GD, Akin JD, et al. 2014. The Interface Region Imaging Spectrograph (IRIS). *Sol Phys* **289**: 2733–2779. https://doi.org/10.1007/s11207-014-0485.

De Toma, G, White OR, Knapp BG, Rottman GR, Woods TN. 1997. Mg II core-to-wing index: comparison of SBUV2 and SOLSTICE time series. *J Geophys Res* **102 (A2)**: 2597–2610. https://doi.org/10.1029/96jA03342.

Dudok de Wit, T, Kretzschmar M, Lilensten J, Woods T. 2009. Finding the best proxies for the solar UV irradiance. *Geophys Res Lett* **36**: L10107. https://doi.org/10.1029/2009GL037825.

Eparvier, FG, Jones AR, Chamberlin PC, Woods TN, McClintock WE, Snow M. 2009. The extreme ultraviolet sensor (EUVS) for GOES-R. *Proc SPIE* **7438**: 4-1–4-8. https://doi.org/10.1117/12.826445.

Ghosh, A, Chatterjee S, Khan AR, Tripathi D, Ramaprakash AN, et al. 2016. The Solar Ultraviolet Imaging Telescope onboard Aditya-L1. *Proc SPIE* **9905**: 11. https://doi.org/10.1117/12.2232266.

Hall, LA, Anderson GP. 1988. Instrumental effects on a proposed Mg II index of solar activity. *Ann Geophys* **6**: 531–534. https://doi.org/10.1029/93JD00421.

Hall, LA, Anderson GP. 1991. High resolution solar spectrum between 2000 and 3100 A. *J Geophys Res* **96**: 12927–12931. https://doi.org/10.1029/91JD01111.

Heath DF, Schlesinger BM. 1986. The Mg 280-nm doublet as a monitor of changes in solar ultraviolet irradiance. *J Geophys Res* **91 (8)**:8672–8682. https://doi.org/10.1029/JD091iD08p08672.

Kayshap, P, Tripath D, Solanki SK, Peter H. 2018. Quiet-Sun and coronal hole in Mg II k line as observed by IRIS. *Astrophys J* **864 (21)**: 12. https://doi.org/10.3847/1538-4357/aad2d9.

Lean JL, Rottman GJ, Lee K, Woods TN, Hickey JR, Puga LC.. 1997. Detection and parameterization of variations in solar mid- and near-ultraviolet radiation (200–400 nm). *J Geophys Res* **102**:29939–29956. https://doi.org/10.1029/97JD02092.

Lean, JL, Coddington O, Marchenko SV, DeLand MT. 2020. A new model of solar ultraviolet irradiance variability with 0.1–0.5 nm spectral resolution. *Earth Space Sci* **9 (10)**: e2021EA002211. https://doi.org/10.1029/2019EA000645.

Machol, J, Eparvier F, Viereck R, Woodraska D, Snow M, et al. 2020. GOES-R series solar X-ray and Ultraviolet Irradiance. In: Goodman S, Schmit T, Daniels J, Redmon RJ (Eds.), *The GOES-R Series: A new generation of geostationary environmental satellites*. Elsevier, Amsterdam, pp. 233–242. https://doi.org/10.1016/B978-0-12-814327-8.00019-6.

Marchenko, SV, Woods TN, DeLand MT, Mauceri S, Pilewskie P, Haberreiter M. 2019. Improved Aura/OMI solar spectral irradiance: comparisons with independent datasets and model predictions. *Earth Space Sci* **6**: 2379–2396. https://doi.org/0.1029/2019EA000624.

McClintock, WE, Rottman GJ, Woods TN. 2005. SOLar STellar Irradiance Comparison Experiment II (SOLSTICE II): instrument concept and design. *Sol Phys* **230**: 225–258. https://doi.org/10.1007/s11207-005-7432-x.

McClintock, WE, Rusch DW, Thomas GE, Merkel AW, Lankton MR, Drake VA, Bailey SM, Russell JM, III. 2009. The cloud imaging and particle size experiment on the aeronomy of ice in the mesosphere mission: Instrument concept, design, calibration, and on-orbit performance. *J Atmos Solar-Terr Phys* **71**: 340. https://doi.org/10.1016/j.jastp.2008.10.011.

McClintock, WE, Snow M, Eden TD, Eparvier FG, Machol JL, Woodraska DL. 2025. High precision, high time-cadence measurements of the MgII Index of solar activity by the GOES-R Extreme Ultraviolet Irradiance Sensor 2: initial flight performance. *J Space Weather Space Clim* **15**: 11. https://doi.org/10.1051/swsc/2025006.

Otter, G, Dijkhuizen N, Vosteen A, Brinkers S, Gür B, Kenter P, et al. 2017. On-ground re-calibration of the GOME-2 Satellite Spectrometer Series. *SPIE* **10564**: 105643G. https://doi.org/10.1117/12.2309063.

Pollock, RE. 1977. Indiana university cyclotron facility – the first year of operation. *IEEE Trans Nuc Sci* **24 (3)**: 1505–1508.

Richard, E, Coddington O, Harber D, Chambliss M, Penton S, et al. 2024. Advancements in solar spectral irradiance measurements by the TSIS-1 spectral irradiance monitor and its role for long-term data continuity. *J Space Weather Space Clim* **14**: 10. https://doi.org/10.1051/swsc/2024008.

Richard, E, Harber D, Rutkowski J, O'Malia K, Triplett M, et al. 2012. Future long-term measurements of solar spectral irradiance by the TSIS spectral irradiance monitor: improvements in measurement accuracy and stability. In: Ikonen E, Park S (Eds.), *Proceedings 11th International Conference on New Developments and Applications in Optical Radiometry*, Vol. 49: Metrologia: Maui, HI, USA, pp. 5–6.

Richard, E, Harber D, Coddington O, Drake G, Rutkowski J, Triplett M, Pilewskie P, Woods T. 2020. SI-traceable spectral irradiance radiometric characterization and absolute calibration of the TSIS-1 Spectral Irradiance Monitor (SIM). *Remote Sens* **12**: 1818–1845. https://doi.org/10.3390/rs12111818.

Rottman, GR, Woods TN, Sparn TP. 1993. Solar stellar irradiance comparison experiment I: 1 instrument design and operation. *J Geophys Res* **98 (10)**: 10679–10694. https://doi.org/10.1029/93JD00463.

Rottman, GR. 2005. The SORCE mission. *Sol Phys* **230**: 7–25. https://doi.org/10.1007/s11207-005-8112-6.

Snow, M, McClintock WE, Woods TN, White OR, Harder JW. 2005. SOLar STellar Irradiance Comparison Experiment II (SOLSTICE II): The Mg II Index from SORCE. *Sol Phys* **230**: 325–https://doi.org/10.1007/s11207-005-6879-0.

Snow, M, McClintock WE. 2005. High time cadence solar magnesium II index monitor. *Proc SPIE* **5901**: 354. https://doi.org/10.1117/12.617044.

Snow M, McClintock WE, Crotser D, Eparvier FG. 2009. EUVS-C: the measurement of the Magnesium II Index for GOES-R EXIS. *Proc SPIE* **7438**: 743803. https://doi.org/10.1117/12.828566.

Snow, M, Weber M, Machol J, Viereck R, Richard E. 2014. Comparison of Magnesium II core-to-wing ratio observations during solar minimum 23/24. *J Space Weather Space Clim* **4**: A04. https://doi.org/10.1051/swsc/2014001.

Snow, M, Machol J, Eparvier F, Jones A, McClintock W, Woods T. 2018. Magnesium II index measurements from SORCE SOLSTICE and GOES-16 EUVS. *Proc Int Astron Union* **13 (S340)**: 167–168. https://doi.org/10.1017/S174392131800128X.

Snow, M, Machol J, Viereck R, Woods T, Weber M, Woodraska D, Elliott J. 2019. A revised Magnesium II core-to-wing ratio from SORCE SOLSTICE. *Earth Space Sci* **2**: 2106–2114. https://doi.org/10.1029/2019EA000652.

Snow, M, McClintock WE, Woods TN, Elliott JP. 2022. SOLar-Stellar Irradiance Comparison Experiment II (SOLSTICE II): End-of-mission validation of the SOLSTICE technique. *Sol Phys* **297**. 55. https://doi.org/10.1007/s11207-022-10984-9.

Thuillier, G, Bruinsma S. 2001. The Mg II index for upper atmosphere modelling. *Ann Geophys* **19**: 219. https://doi.org/10.5194/angeo-19-219-2001.

Viereck, RA, Puga LC, McMullin D, Judge D, Weberand M, Tobiska WK. 2001. The Mg II index: a proxy for solar EUV. *Geophys Rev Lett* **28 (7)**: 1343–1346. https://doi.org/10.1029/2000GL012551.

Viereck, R, Floyd L, Crane P, Woods T, Knapp B, Rottman G, Weber M, Puga L, DeLand M. 2004. A composite Mg II index spanning from 1978 to 2003. *Space Weather* **2**: S10005. https://doi.org/10.1029/2004SW000084.

White, OR, De Toma G, Rottman GJ, Woods TN, Knapp BG. 1998. Effect of spectral resolution on the Mg II Index as measure of solar variability. *Sol Phys* **177**: 89–103. https://doi.org/10.1007/978-94-011-5000-2_7.

Wintoft, P. 2011. The variability of solar EUV: A multiscale comparison between sunspot number, 10.7 cm flux, LASP MgII index, and SOHO/SEM EUV flux. *J Atmos Sol-Terr Phys* **73 (13)**: 1708–1714. https://doi.org/10.1016/j.jastp.2011.03.009.

Woods, TN, Eparvier FG, Hock H, Jones AR, Woodraska D, et al. 2012. Extreme Ultraviolet Variability Experiment (EVE) on the Solar Dynamics Observatory (SDO): overview of science objectives, instrument design, data products, and model developments. *Sol Phys* **275**: 115–143. https://doi.org/10.1007/s11207-009-9487-6.

Woods, TN, Eparvier FG, Harder J, Snow M. 2018. Decoupling solar variability and instrument trends using the Multiple Same-Irradiance-Level (MuSIL) analysis technique. *Sol Phys* **293 (5)**: 76–96. https://doi.org/10.1007/s11207-018-1294-5.

Woods, TN, Eden E, Eparvier FG, Jones AR, Woodraska DL, Chamberlin PC, Machol JL. 2024. GOES-R Series X-Ray Sensor (XRS): 1. design and pre-flight calibration. *J Geophys Res Space Phys* **129 (11)**: e2024JA032925. https://doi.org/10.1029/2024JA032925.

Yeo, KL, Krivova NA, Solanki SK. 2017. EMPIRE: A robust empirical reconstruction of solar irradiance variability. *J Geophys Res Space Phys* **122 (4)**: 3888–3914. https://doi.org/10.1002/2016JA023733.

**Cite this article as**: McClintock WE, Snow M, Crotser D & Eparvier FG. 2025. High precision, high time-cadence measurements of the Mg II index of solar activity by the GOES-R extreme ultraviolet irradiance sensor 1: EUVS-C design and preflight calibration. *J. Space Weather Space Clim.* **15**, 12. https://doi.org/10.1051/swsc/2025005.